Polymer Testing 153 (2025) 109019

Contents lists available at ScienceDirect

Polymer Testing

journal homepage: www.elsevier.com/locate/polytest

Effect of high-temperature high-speed airflow on the thermo-oxidative aging of epoxy polymer and composite: An experimental study

Aurélien Doriat [a,*], Marco Gigliotti [b], Marianne Beringhier [c], Gildas Lalizel [a], Eva Dorignac [a], Patrick Berterretche [a], Matteo Minervino [d]

[a] Institut Pprime, CNRS, ISAE-ENSMA, Universite de Poitiers, 1, Avenue Clement Ader, BP 40109, Chasseneuil Futuroscope, 86961, France
[b] University of Pisa, Dipartimento di Ingegneria Civile e Industriale (DICI), Via G. Caruso 8, Pisa, 56122, Italy
[c] Arts et Metiers Institute of Technology, LAMPA, Angers, F-49035, France
[d] Safran Aircraft Engine – SAFRAN Group, Rond Point Rene Ravaud – Reau, Moissy Cramayel Cedex, 77550, France

ARTICLE INFO

Keywords:
Thermo-oxidation
Airflow
Polymer
Composite
Experimental study

ABSTRACT

The objective of this study is to investigate the effect of the airflow on the thermo-oxidative aging of polymer matrix composites (PMCs). Understanding how airflow affects the aging process is crucial for designing composite parts subjected to airflow conditions, such as in aeronautics. We conducted tests in an oven at 150 °C and in wind tunnel at Mach 0.85 to compare static and dynamic aging conditions. The airflow conditions are determined using a Reynolds Averaged Navier–Stokes (RANS) Computational Fluid Dynamic (CFD) simulation to estimate the pressure and temperature conditions at any point of the air-polymer interface. The oxidation is characterized by colorimetric and roughness testing. Based on our experimental data and simulation results, we show that the compressibility effect of the airflow affects the pressure field at the interface and the thermal boundary layer affects the temperature of the samples. The samples aged in the wind tunnel are always more oxidized than those aged under oven conditions. The airflow accelerates the thermo-oxidation by mainly increasing the static pressure.

1. Introduction

Aeronautical structures include more Polymer Matrix Composites (PMCs) to reduce mass [1]. Some parts, such as fan blades in turbojet engines, experience extreme operating conditions for matrix polymer, mostly with epoxy. These conditions include exposure to high-speed air flows near Mach 1 ans elevated temperatures above 90 °C, which lead to oxidative environments that accelerate material degradation [2,3]. The chemical modifications during degradation induce a color change [4] and chemical shrinkage. Those modifications also affect the mechanical properties [5–7]. The ability of PMCs to perform under such conditions while maintaining mechanical integrity is essential for ensuring the safety and efficiency of aerospace systems.

However, traditional studies of PMC aging have primarily been conducted in static air environments, where the effects of temperature and pressure on oxidation are well-characterized [8]. Thermo-oxidation is a reaction–diffusion mechanism. The temperature impacts the oxygen diffusivity and the reaction kinetics following an Arrhenius law. Near the glass transition temperature, oxidation is significantly enhanced [2,9,10]. Other mechanisms can be enhanced, such as molecular mobility, post-curing, or physical aging; the activation energy can change [11,12]. In the case of diamine epoxy resin, the molecular mobility decreases the rate constants of the elementary reactions involving the peroxy radicals. When passing from rubbery to glassy state, the rate constants of the Arrhenius laws of these reactions decrease, up to five orders of magnitude, which significantly accelerates the oxidation near the glass transition temperature [11]. The pressure affects the oxygen concentration at the interface. Oxidation is directly linked to the amount of oxygen at the sample surface, and higher oxygen partial pressures enhance the uptake of oxygen within the material [13]. Increasing pressure is an effective way to accelerate oxidation and reduce experimental durations [14]. It accelerates oxidation for some polymers (e.g., PP, PA, CR) but not for others (e.g., PE), and the critical pressure depends on temperature and usually decreases with increasing temperature [15]. For epoxy thermosets, the acceleration effect saturates at higher pressures [16]. The authors show saturation from 5 bar of air depending on the temperature and the material. In addition, elevated pressures significantly alter the thickness of the oxidized layer and cause deeper mechanical degradation, such as reduced elongation at break [17]. The surrounding environment is accounted for through oxygen boundary conditions for thermo-oxidation, based on chemical

* Corresponding author.
E-mail addresses: aurelien.doriat@ensma.fr (A. Doriat), marco.gigliotti@unipi.it (M. Gigliotti).

https://doi.org/10.1016/j.polymertesting.2025.109019
Received 24 July 2025; Received in revised form 13 October 2025; Accepted 27 October 2025
Available online 29 October 2025
0142-9418/© 2025 The Author(s). Published by Elsevier Ltd. This is an open access article under the CC BY-NC license (http://creativecommons.org/licenses/by-nc/4.0/).

potential equilibrium [18]. This equilibrium results in Henry's law, Eq. (1) gives the oxygen concentration at the interface $[O_2]_0$, with S representing the solubility of oxygen in the material and P_{O_2} the partial pressure of oxygen in the air.

$$[O_2]_0 = S \cdot P_{O_2} \tag{1}$$

Henry's law is commonly used [11,19]. This boundary condition remains valid until the material is saturated with oxygen—a threshold that depends on the polymer, but can occur around 1 bar [20]. Until saturation, Henry's law can be used to describe the linear relationship between the partial pressure of oxygen and the oxidation rate.

Alternative models, such as logarithmic [20] or Langmuir's law, account for higher pressure and saturation [21] have also been used. Fluid flow can alter these conditions, impacting predictions of chemical and mechanical changes during aging. These controlled conditions do not replicate the complexities of in-service environments, where high-speed aerothermal flows introduce modifications of the thermo-oxidation process.

The airflow could create shear stress, affect pressure field through compressibility effects, and cause heat flux due to temperature field in thermal boundary layer at the fluid-solid interface. Indeed, compressibility effects become significant when the Mach number (Ma), the ratio of flow velocity to the speed of sound, exceeds 0.6. In subsonic flows, the total temperature T_t and the total pressure P_t remain constant, leading to variation between the static temperature T, static pressure P_s and the Mach number (See Eqs. (2) and (3) where γ is the ratio of specific heats) [22,23].

$$\frac{T_t}{T} = 1 + \frac{\gamma - 1}{2} Ma^2 \tag{2}$$

$$\frac{P_t}{P_s} = \left(1 + \frac{\gamma - 1}{2} Ma^2\right)^{\frac{\gamma}{\gamma - 1}} \tag{3}$$

The boundary layer, a near-wall region dominated by viscous effects, is critical for heat transfer, and mass exchange between the fluid and the solid [24]. Thermal and mass boundary layers are also created, characterized by temperature and concentration gradients. These gradients could influence convective heat and mass fluxes. An analogy between thermal and mass transfer can help to estimate these fluxes [25]. The pressure of the surrounding and the temperature of the polymer or composite could impact the thermo-oxidation through the aero-thermal-mechanical coupling.

Only few articles deal with the effect of a flow on the polymer degradation. Some studies can be found on the effect of the salinity and corrosion to polymer coating under marine wind. In this case, authors have shown that near-wall shear and mass transfer (water, ions, and pollutants) accelerate corrosion in epoxy coatings, while flow also affects coating thickness through swelling and erosion [26,27]. Increased pressure further intensifies aging [28]. Also, chlorinated water or disinfectants can degrade polymer pipe. These chemical reactions enhance degradation due to flow dynamics, including velocity and flow rate, facilitating mass transfer of reactants like oxygen and chlorine dioxide, and intensifying mechanical stresses that accelerate failure mechanisms or create microplastic inside the water [29,30].

All these studies lead to show an impact of the flow environment on the aging of the coating.

Therefore, this paper aims to address the research gap in understanding the effect of an high-speed (close to the sonic speed) heated airflow on the thermo-oxidation of diamine-epoxy polymer. The primary objective is to estimate the modifications of the pressure and temperature fields at the interface between the sample and the airflow. By comparing samples aged in static conditions (oven) and dynamic conditions (wind tunnel), we seek to understand how the oxidation kinetics are affected by the airflow. This study advances existing knowledge by establishing an oxygen boundary condition for sample aged under a high temperature and high speed airflow, which can be used for modeling purposes. Two kinds of samples will be used in this experimental study, polymer samples and composite ones. For composite samples, only the polymer matrix is studied as the carbon fibers do not undergo thermo-oxidation. To assess the impact of an airflow on the sample surface, roughness measurements will be conducted to quantify the changes and determine whether airflow affects it. Additionally, comparative analyses between samples aged in static conditions (oven) and dynamic conditions (wind tunnel) will be performed using color difference tests. This colorimetric test has been validated using indentation tests [31]. This experimental study will provide insights into the material's color change and oxidative layer thickness enabling a deeper understanding of how flow conditions contribute to material aging. First, a description of the wind tunnel and fluid simulation will be presented to set the aging temperature and pressure conditions. Then, the characterization method of the oxidation level will be presented to later compare samples oxidized layer between oven and wind tunnel aging. Finally, the airflow effect will be discussed and an oxygen boundary condition will be established.

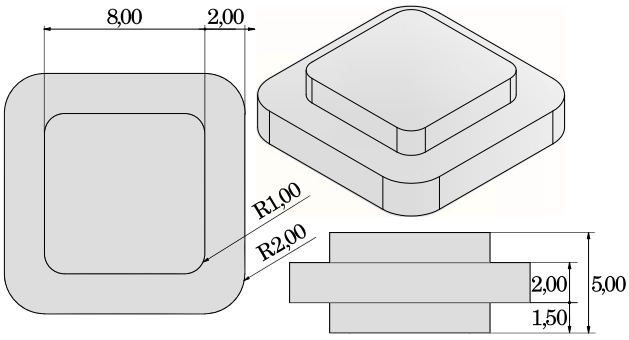

Fig. 1. Plan of the sample illustrating the geometry, dimensions, and positioning within the experimental setup (in mm).

2. Materials and characterization method

2.1. Materials

The polymer used in this study is a PR520RTM epoxy-diamine resin manufactured by Cytec Engineered Materials (similar to [32]). The glassy transition temperature of the virgin polymer is 155 °C [32]. The curing and shaping were entirely performed by SAFRAN, and the samples were received in their final shape and polymerized.

Composite samples will also be used in this study. These composites are composed of woven carbon fibers and a polymer matrix identical to that of the polymer samples. For confidentiality reasons, the weaving pattern is not provided. The shape of the composite samples is identical to that of the polymer samples for both oven and wind tunnel aging tests to ensure that geometry has no influence on the oxidation process. The plan of the sample is shown in Fig. 1.

The position of the samples in the sample holder is shown in Fig. 2. Both composite and polymer samples are in the middle row to have an homogeneous temperature in the sample. Samples on the lateral row undergo temperature gradient due to conductive losses in the test ring.

2.2. Roughness

Roughness measurements on the surface exposed to the environment were conducted using an Alicona Infinite Focus microscope, following ISO 4287 and ISO 4288 standards. The microscope measures the arithmetic mean roughness (R_a) by measuring the elevation z along the surface x as:

$$R_a = \frac{1}{l} \int_0^l |z(x)| dx \tag{4}$$

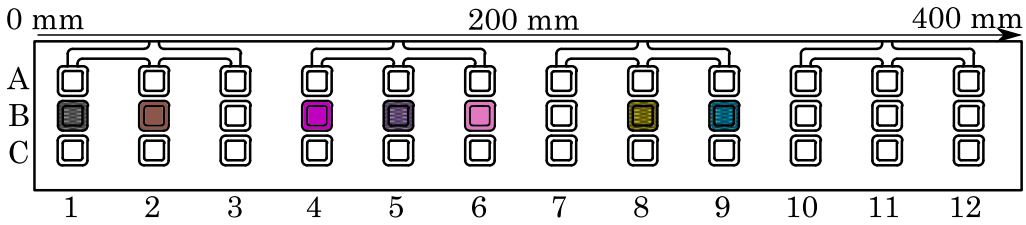

Fig. 2. Samples holder with the position of polymer (2,4,6) and composite (1,5,8,9) used in this study. The color assigned to each sample will remain consistent throughout all figures.

The roughness measurement process involves the following steps:

First, the surface is reconstructed in 3D by adjusting brightness and contrast to bring all points into focus. The vertical (R_v) and lateral (R_l) resolutions depend on the surface roughness, with finer resolutions yielding more precise measurements at the cost of longer acquisition times. For accurate measurements, the following conditions must be satisfied:

$$R_v < \frac{R_q}{2.5} \quad ; \quad R_l < \frac{R_{sm}}{10}$$

where R_q is the quadratic roughness and R_{sm} is the square mean roughness. Next, the general shape of the profile is removed to eliminate any tilt or global surface form that could affect roughness measurements. In this study, surfaces showed no specific global form but often had slight inclinations. A third-order polynomial was used to subtract the overall profile.

Finally, a filter is applied to separate surface waviness from roughness. This filter, characterized by the parameter L_c, removes all surface features with a characteristic size greater than L_c. This filter also determines the minimum profile length required for measurements. For the samples in this study, roughness remained below 2 µm, and a cutoff parameter $L_c = 800\,\mu m$ was predominantly used. Profiles analyzed were approximately 5 mm long. Each measurement of roughness is the average of six measurements. In the plot, the vertical bar is the standard deviation of these six measurements.

2.3. Colorimetry

The color difference ΔE^*_{ab} is used in this paper to quantify the oxidation evolution and to compare the samples aged in different environments. The colorimetric methodology has been previously developed [31] and compared with indentation measurements.

Images were captured using a Feyence VHX-7000 optical microscope equipped with a dual lens at a magnification of x20. The microscope's camera is equipped with a CMOS sensor offering a resolution of 6144×4608 pixels, corresponding to 2.5 µm per pixel. Each pixel features a dynamic range of 16 bits. Illumination was set to 4 ms using an LED ring light, optimizing the color range to distinguish between unoxidized (white) and oxidized (black) samples. All images were saved in uncompressed sRGB TIFF format.

For each pixel, sRGB color coordinates were extracted and converted to CIELAB coordinates using the OpenCV library in Python. The CIELAB color space is more uniform with respect to human eye sensitivity. In CIELAB color space, L^* represents lightness, a^* corresponds to the green-magenta axis, and b^* corresponds to the blue-yellow axis.

The color difference ΔE^*_{ab} between two samples, such as an unoxidized reference sample v and an aged sample s, is calculated using the Euclidean norm between their color coordinates, as defined in Eq. (5). A color difference $\Delta E^*_{ab} = 2$ is detectable by the human eye.

$$\Delta E^*_{ab} = \sqrt{(L_v - L_s)^2 + (a_v - a_s)^2 + (b_v - b_s)^2} \tag{5}$$

The color difference will be used to follow the oxidation level at the sample interface.

3. Oven and wind tunnel aging conditions

3.1. Oven aging condition

Samples aged inside the oven were exposed to air at atmospheric pressure ($P_{O_2} = 0.21$ bar) at 150 °C between 10 h and 1000 h. Each sample was exposed to temperature and oxygen in the oven, and surface roughness and color measurements were performed at specific aging times to monitor oxidation. The temperature was chosen to faster the aging as the experiment in a wind tunnel is highly costly and time consuming. The glassy temperature of the polymer is between 155 °C et 160 °C [11,32]. In the case of the diamine epoxy, the thermo-oxidation mechanism (chemical reactions) remains the same. Aging close (or above) to the glass temperature will only faster the oxydation reaction as demonstrate by Colin et al. [11]. In addition of the bibliography, we performed nitrogen aging at 150 °C. Nitrogen aging does not show variations in mechanical properties or color, suggesting that our material is not subject to any other phenomenon than thermo-oxidation for the exposure duration.

3.2. BATH wind tunnel aging condition

The BATH (Banc AéroTHermique) wind tunnel was used, and the test section was adapted to age the polymer and composite samples. Fig. 3 illustrates the main components of the test section of the wind tunnel. More details of the facilities can be found in [33]. The flow is heated using an electric heater of 250 kW. Hot air first passes through a convergent (on the left in the figure) to reduce the cross-sectional area and accelerate the flow. The test section has a passage width of 50 mm and a height of 16 mm. The rate flow is around 300 g s^{-1} at a total temperature of 158 °C. This total temperature is chosen to expose the samples at a temperature close to 150 °C (Eq. (2)). A sample holder divides the flow into two symmetrical sections and can accommodate up to 36 samples simultaneously in three columns of 12 samples (see Fig. 2). Samples are placed inside a sample holder to ensure that they are exposed to the same flow on both sides (identical oxygen boundary conditions) and maintain a uniform temperature as close as possible to the flow temperature (see Fig. 3). The samples later used to understand the effect of the airflow on the aging are colored. Wind tunnel floors provide a final section reduction to achieve flow conditions close to the speed of sound. As with the samples exposed in the oven, each sample undergoes color measurements at specific aging times and is then placed in the same position in the sample holder.

3.2.1. Total pressure measurement

Total pressure measurements are conducted using a Pitot tube with an inner diameter of 0.5 mm and an outer diameter of 1 mm, providing an absolute positioning accuracy of 1 mm. Relative positioning accuracy between two points is ensured by robotic displacement systems with precision below 0.01 mm. The Pitot tube is connected to a pressure sensor with a measurement range from 0 bar to 2.5 bar (PTX 5072 TA A2 CA H0 PA), delivering currents between 4 and 20 mA to measure the total pressure. Each acquisition point averages 20 measurements taken at 10 Hz, over a period of 2 s. The probing plane is at the end of the sample holder inside the test section.

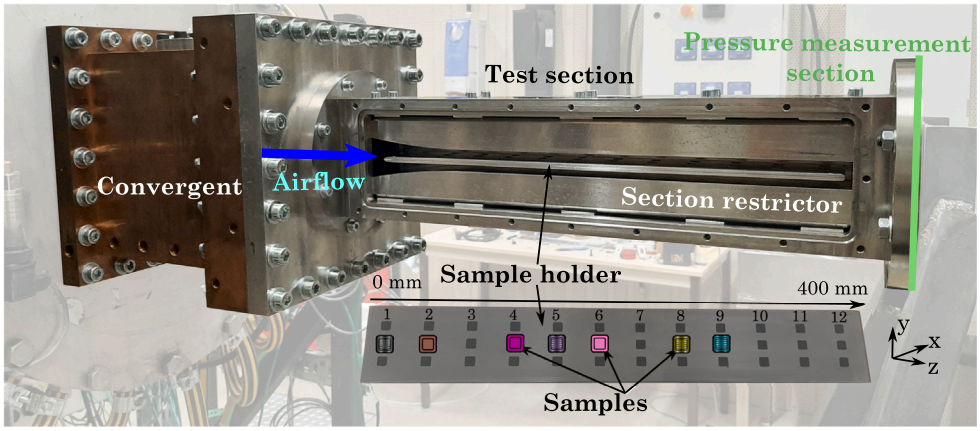

Fig. 3. Wind tunnel experimental setup picture. The airflow goes through a convergent and between to section restrictor to increase the velocity. In the middle of the test section, samples are aged. The samples later used to understand the effect of the airflow on the aging is colored.

3.2.2. Sample temperature measurement

Sample temperature measurements are performed using a K-type thermocouple with a diameter of a few tens of micrometers, providing a response time of approximately 10 ms. The thermocouples are inserted inside the sample before curing. Measurements are recorded at 1 Hz, and each data point is an average of 50 measurements. The absolute accuracy of the K-type thermocouple is 1 °C, with a relative accuracy of 0.1 °C.

3.2.3. Airflow simulation

A Reynolds Averaged Navier–Stokes (RANS) simulation was conducted to estimate the temperature in the sample and in the air, as well as the pressure field, to better predict the aging conditions on all samples depending on their position inside the sample holder in the test ring. The aim of this simulation is to estimate the temperature distribution across the sample and the pressure at the interface, as direct measurements of temperature and pressure at such spatial resolution are not feasible. The simulation must be validated at specific points using experimental data before it can be reliably used to support the interpretation of the results. The mass, momentum (Navier–Stokes equation), and energy conservation equations are solved in the fluid domain, while energy conservation is resolved in the solid parts. Natural convection boundary conditions are applied to the solid components of the test section exposed to the external environment ($h = 10\,\mathrm{W\,m^{-2}\,K^{-1}}$, $T_{env} = 300\,\mathrm{K}$ to model the natural convection outside the test ring). The temperature at the surface in contact with the settling chamber (on the right side of the convergent) is fixed at 300 K to reflect its thermal equilibrium.

For the fluid, the $k-\omega$ SST (Shear Stress Transport) Menter turbulence model is employed for compressible flow, using a fine mesh in the near-wall region ($Y^+ < 1$) to accurately simulate boundary layers and thermal exchange coefficients. This turbulence model is chosen to obtain an accurate modeling of turbulence near the wall with the $k-\omega$ turbulence model. Further from the wall, the $k-\epsilon$ model accurately predicts turbulence. The inlet fluid conditions include a total pressure P_t of 1.85 bar and a total temperature T_t of 434 K which are the values used in the aging experiments. The turbulence intensity is set to 5%, based on data from [33]. At the outlet, the static pressure is set to the atmospheric pressure, 1 bar, as it is an open wind tunnel, and the static temperature is estimated at 400 K using Eqs. (3) and (2). All the boundary conditions and the geometry of the CFD calculation are summarized in the Fig. 4.

The simulation is performed using StarCCM+ software with a mesh comprising 34 million cells, including 25 prism layers in the boundary layer region with a growth factor of 1.2 over 1.25 mm. The computation, executed on 48 CPUs (Intel Xeon Gold 6252 @ 2.10 GHz) with 8 GB RAM per CPU, requires approximately 10 h.

3.2.4. Wind tunnel characterization and simulation validation

In Figs. 5(a) and 5(b), the total pressure profiles obtained from numerical simulation (line) and experimental (dot) results show good agreement. The simulation overestimates the total pressure at the center of the test section by approximately 5%, which is considered acceptable. The error of RANS simulation depends on the turbulence closure model. The $k-\omega$ SST turbulence model is the most appropriate two-equation model for heat transfer simulation [34]. Additionally, the dynamic boundary layer thickness predicted by the simulation is underestimated as seen in the wake of the sample holder, likely due to weaker turbulence development in the simulation compared to the test section, which has assembly gaps that are not modeled. These gaps create small recirculation vortices which increase the turbulence and so the boundary layer. Consequently, the simulated heat transfer is slightly overestimated because the simulated boundary layers are thinner, leading to steeper temperature gradients and enhanced exchange.

Fig. 6 shows the temperature in the middle of the sample holder. The results from the simulation are plotted in black and in color, red or blue, the measurements with the thermocouple. The trend of decreasing temperature with distance from the leading edge of the sample holder is well captured. This decrease is due to a thickening of the boundary layer, which reduces the temperature gradient near wall and thus the heat transfer. However, a consistent overestimation is observed across all temperatures. The error is less significant for the sample at the side row, and the biggest error is for the sample at the end of the sample holder, which can be influenced by the wake of the sample holder and the conductive losses. The simulated temperature is overestimated by approximately 2 °C on the middle row near the position of the exposed samples. Side rows exhibit symmetrical temperature distributions. Overall, there is good agreement between the simulated and experimentally measured temperatures. Finally the temperature used to analyze the samples will be extracted from the simulation minus this error.

These results validate the numerical simulation results with experimental pressure and temperature measurements. The pressure, and consequently the Mach number, varies linearly with the sample positions. It is worth noting that the wind tunnel is controlled in terms of flow rate and total temperature. For this reason, precise control over the conditions experienced by the samples is limited. Nonetheless, the aerothermal simulation accurately predicts the pressure and temperature at the sample locations, supporting its validation.

Table 1 summarizes the temperature and pressure conditions experienced by the samples in the central row of the sample holder. The error between the simulation and experimental measurements in the pressure and temperature field should be keep in mind as these values will be used to discuss the results.

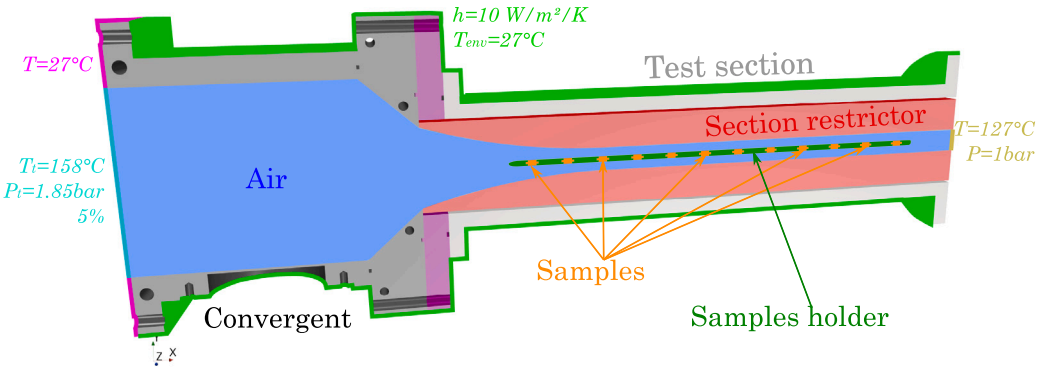

Fig. 4. 3D model used in the RANS simuation with the boundray conditions used. The solid and the fluid is modeled.

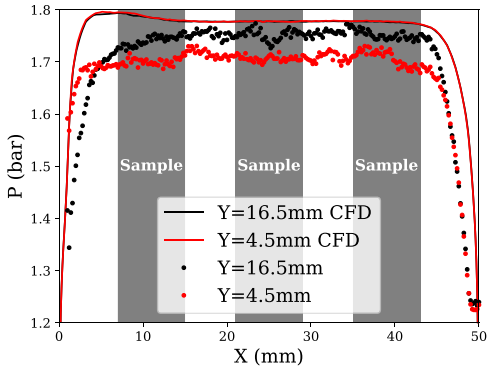

(a) Comparison between measured and simulated pressure profiles at the test section exit. Shaded areas represent sample positions.

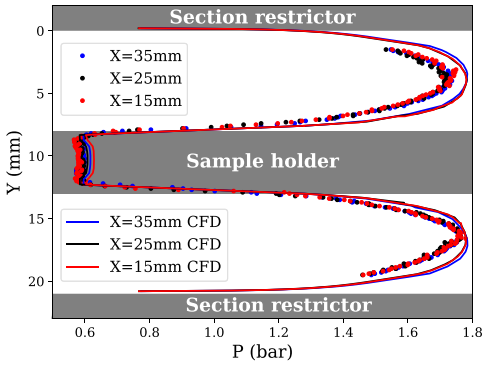

(b) Comparison between measured and simulated pressure profiles at the test section exit. The shaded area represents the sample holder position.

Fig. 5. Comparison of measured (dot) and calculated (line) pressure profiles.

Table 1
Corrected temperature, pressure, velocity and Mach number conditions for samples in the central row of the sample holder. Colors correspond to the studied central samples in subsequent sections (see Fig. 3).

Position		Temperature	Pressure	Velocity	Mach number
1	20 mm	152.9 °C	1.70 bar	130 m s^{-1}	0.31
2	53 mm	151.8 °C	1.54 bar	201 m s^{-1}	0.49
4	119 mm	150.9 °C	1.33 bar	273 m s^{-1}	0.68
5	152 mm	150.7 °C	1.29 bar	286 m s^{-1}	0.72
6	185 mm	150.4 °C	1.26 bar	295 m s^{-1}	0.75
8	251 mm	149.8 °C	1.18 bar	319 m s^{-1}	0.81
9	283 mm	149.4 °C	1.14 bar	330 m s^{-1}	0.85

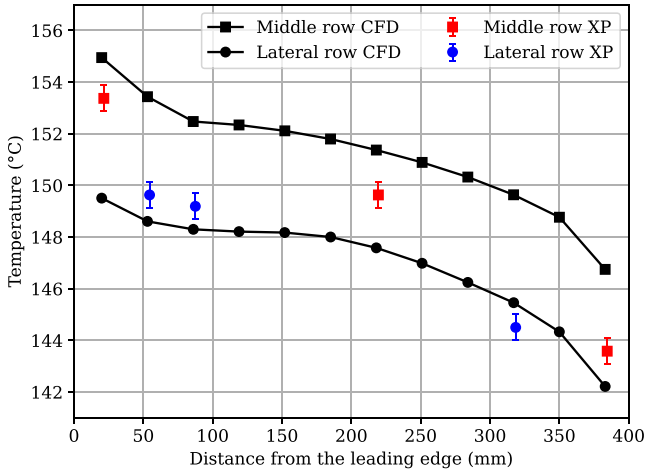

Fig. 6. Comparison of temperature profiles along the leading-edge distance between simulation results and experimental measurements for samples at a total temperature of 161 °C.

4. Experimental comparison of aged samples in oven and wind tunnel

4.1. Interface characterization

As airflow can alter the surface of the sample or enhance oxygen transfer at the interface, roughness measurements are taken and mass transfer is estimated.

4.1.1. Roughness measurements

The airflow could affect the sample by changing the roughness due to friction force or increase the oxygen inside the sample by mass transfer.

First, frictional forces at the interface could lead to phenomena such as erosion. On a composite sample, the presence of fibers could exacerbate these effects. The variation of arithmetic roughness R_a as a function of aging time for samples aged in an oven and in a wind tunnel is presented in Fig. 7.

Fig. 7 shows two initial roughness levels studied in the wind tunnel, comparable to those investigated in the oven. Different levels of initial roughness are obtained using sandpaper. The variation in roughness

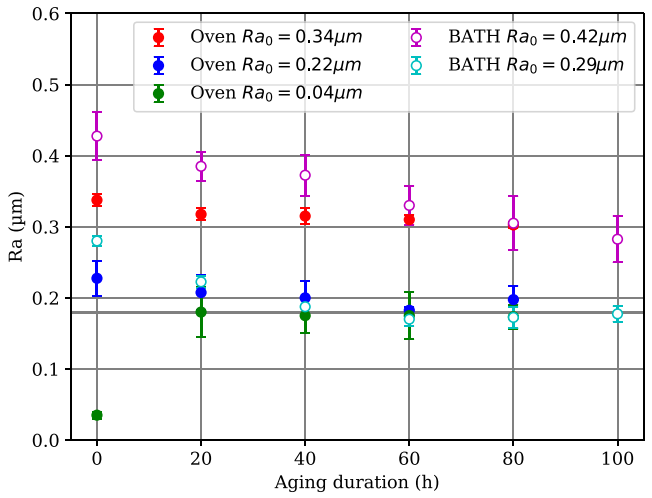

Fig. 7. Variation of roughness as a function of time for samples aged in a wind tunnel (magenta and cyan) and in an oven (red, blue, and green).

is similar to what is observed during oven aging due to changes in chemical bonds and groups. Studies have shown a relationship between crosslinking, chain scission, and surface roughness in various polymer families [35,36]. For instance, in polystyrene (PS), roughness decreases with the formation of a continuous crosslinked layer, whereas in poly(methyl methacrylate) (PMMA), roughness increases. Surface roughness is attributed to polymer aggregation associated with crosslinking. The balance between crosslinking and chain scission is critical: roughness peaks when their rates are comparable and drops to negligible levels at very low or very high crosslinking rates [36]. At very low crosslinking rates, aggregation is minimal, resulting in low roughness. Conversely, at very high crosslinking rates, a continuous crosslinked surface layer forms, also leading to low roughness.

In our case, roughness decreases with oxidation for both initial roughness levels. The decrease in roughness at the surface suggests that crosslinking or chain scission is dominant in our materials. For samples with an initial roughness of 0.29 µm, the decrease stabilizes at the same asymptotic value of 0.18 µm observed in the oven. Samples with a higher initial roughness of 0.42 µm exhibit a monotonic decrease with exposure time, with a steeper decline compared to oven aging, which may indicate accelerated aging kinetics. The airflow accelerates the decrease in surface roughness but does not seem to cause erosion; unlike particle erosion, air does not tear material off as all air particles are stopped at the interface in the boundary layer due to viscous effects.

4.1.2. Mass transfer estimation

The mass transfer can be estimated with the Chilton–Colburn analogy [24,25] (Eq. (6)) based on the heat transfer coefficient h and the mass transfer coefficient h_{mass}. These exchange coefficients are linked by various parameters dependent on the fluid and the material through relation given in Eq. (6), with D_{AB} being the oxygen diffusion coefficient in the solid, α the thermal diffusivity, λ the thermal conductivity, ρ the volumetric mass, and C_p the specific heat capacity of the fluid. The Lewis number $Le = \frac{\alpha}{D_{AB}}$ translates the interplay between heat diffusion and mass diffusion. When Le equals 1, the boundary layers overlap.

$$h_{\text{mass}} = \frac{h}{\rho C_p} Le^{-2/3} = \frac{h}{\rho C_p} \left(\frac{D_{AB}}{\alpha} \right)^{2/3} \tag{6}$$

The thermal diffusivity of the polymer is $\alpha = \frac{\lambda}{\rho C_p} = \frac{0.25}{1.2\times10^3\times1.2\times10^3} \approx 1.7 \times 10^{-7}\,\text{m}^2/\text{s}$.

To calculate the Lewis number, the oxygen diffusion coefficient is estimated at 150 °C [11]. The Lewis number is $Le = \frac{\alpha}{D_{AB}} = \frac{1.7\times10^{-7}}{1.6\times10^{-12}} \approx 10^5$. Thus, the Lewis number is very large, which means the characteristic time of temperature variation is much higher than that of oxygen diffusion in the material. To quantify the mass transfer, one must estimate the thickness of the oxygen diffusion boundary layer in the material.

The mass boundary layer is illustrated in Fig. 8. In our case, the compressible effect in the flow affect the pressure field, leading to a gradient in the oxygen partial and so in the oxygen concentration.

The thickness of the mass boundary layer δ_{mass} can be expressed as a function of the Schmidt number $Sc = \frac{\nu}{D_{AB}}$, the ratio of momentum diffusivity ν to mass diffusivity D_{AB}. The thickness of the velocity boundary layer δ can be approximated using the CFD simulation and allows estimating the heat exchange coefficient $h \approx 500\,\text{W}\,\text{K}^{-1}\,\text{m}^{-2}$ and the thickness of the velocity boundary layer $\delta \approx 1\,\text{mm}$. Thus, one can estimate the mass exchange coefficient $h_{\text{mass}} \approx 1.5 \times 10^{-7}\,\text{m}\,\text{s}^{-1}$. The thickness of the mass boundary layer $\delta_{\text{mass}} \approx 0.18\,\text{mm}$ is given by Eq. (7).

$$\frac{\delta}{\delta_{\text{mass}}} = Sc^{\frac{1}{3}} = \left(\frac{\nu}{D_{AB}} \right)^{\frac{1}{3}} = 5.4 \tag{7}$$

The characteristic time of mass exchange is given by Eq. (8) for a surface layer.

$$\tau_{\text{mass}} = \frac{\delta_{\text{mass}}^2}{D_{AB}} \approx 2 \times 10^4\,\text{s} \tag{8}$$

Different equivalent times can be considered to characterize oxidation, which is a consequence of oxygen absorption. An estimation of three equivalent times can be done. All the values of the reaction constants used in the following calculations are taken from [11] for the DGEBF-CAF at 150 °C.

First, an oxygen absorption rate is estimated. To have a steady state in the oxidation process, the absorption of oxidation should be fast enough for the propagation reaction $P^\circ + \text{O}_2 \rightarrow PO_2^\circ$, leading to Eq. (9).

$$\tau_{\text{O}_2} = \frac{1}{k_2[\text{O}_2]_0} = \frac{1}{k_2 S_{\text{O}_2} P_{\text{O}_2}} \approx \frac{1}{10^8 \times 10^{-7} \times 10^4} \approx 10^{-6}\,\text{s} \ll \tau_{\text{mass}} \tag{9}$$

Thus, the kinetics of mass transfer are much slower than the kinetics of oxygen absorption.

Then, an oxygen consumption rate could be consider from on the same chemical reaction as Eq. (10). This equation is derivated from [37] with $\beta = \frac{k_6 k_2}{k_5 k_3 [PH]}$.

$$\tau_{r_{\text{O}_2}} = \frac{1}{k_2[P^\circ]} = \frac{2k_5(1+\beta[\text{O}_2]_0)}{k_2 k_3 [PH]} \approx \frac{6 \times 10^{11}}{10^8 \times 3 \times 10} \approx 10^2\,\text{s} \ll \tau_{\text{mass}} \tag{10}$$

This oxygen consumption rate takes into account the absorption and the reaction of the oxygen. Nevertheless, it is still negligible regarding the mass transfer equivalent time.

Finally, an oxidation equivalent time can be computed (Eq. (11)) from the steady state rate r_0 with $r_0 = \frac{k_3^2[PH]^2}{4k_6}$.

$$\tau_{r_{\text{O}_2}} = \frac{1}{2\sqrt{r_0 k_{1b}}} \approx \frac{1}{2\sqrt{10^{-4} \times 10^{-2}}} \approx 10^3\,\text{s} \ll \tau_{\text{mass}} \tag{11}$$

This equivalent time takes into account the absorption and the reaction of the oxygen and the reaction of the other species. Nevertheless, it is still lower than the mass transfer equivalent time.

The presence of rapid airflow during aging does not appear to significantly impact roughness variation, as similar variations and asymptotic values are achieved in the oven. This suggests that erosion or ablation effects caused by fluid friction are negligible on the roughness for these initial roughness levels and with this polymer. In addiction, the calculation shows that the mass transfer of oxygen in the polymer is negligible. Thus, the airflow does not affect the surface of the sample with erosion or mass transfer.

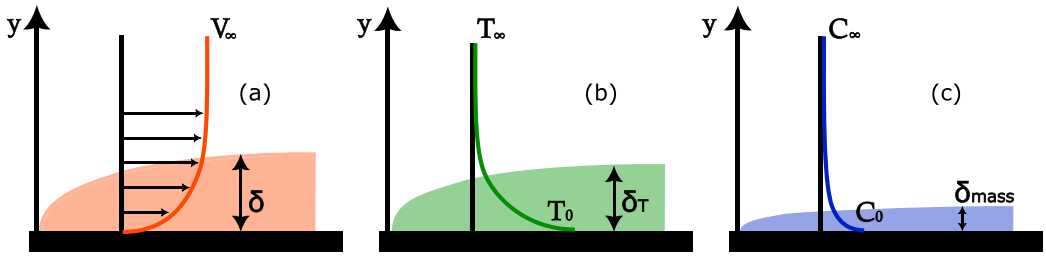

Fig. 8. Boundary layer thickness illustration. The thickness of each boundary layer is when 99% of the bulk value is reached. (a) Velocity boundary layer is created due to viscous effect of the flow as the fluid flow velocity is zero at the solid surface. (b) The thermal boundary layer is a thin film of fluid near a solid surface where the velocity is relatively low, resulting in heat transfer primarily by conduction rather than convection. (c) The mass boundary layer is the near wall region where due to velocity gradient a concentration gradient is created.

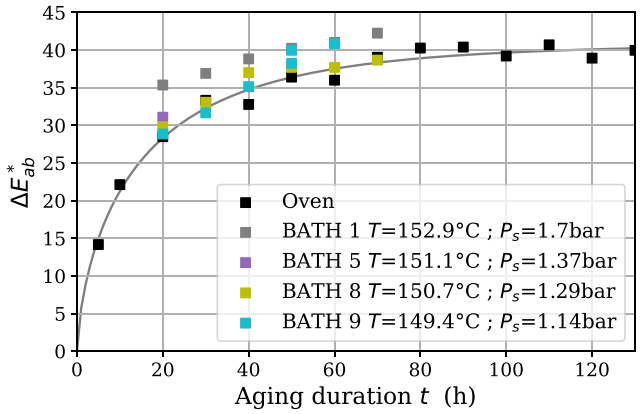

Fig. 9. ΔE^*_{ab} variation against the aging duration at the sample surface for composite samples.

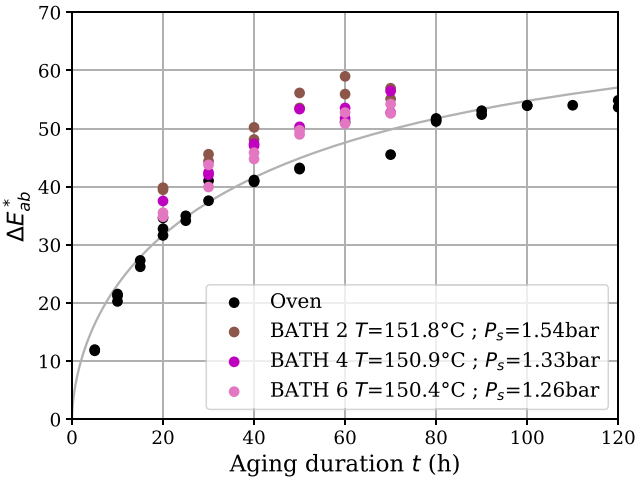

Fig. 10. ΔE^*_{ab} variation against the aging duration at the sample surface for polymer samples.

4.2. Color change results

The color is used to quantify the oxidation level [31]. The yellowing observed in the epoxy is directly caused by the irreversible process of thermo-oxidation, specifically due to carbonyl formation. This makes yellowing a reliable method for characterizing the extent of oxidation [4,38,39]. Figs. 9 and 10 illustrate the variation of color change as a function of exposure time for polymer and composite samples. In black, the samples exposed in the oven are shown and in color, the samples aged in the wind tunnel. The color of the points corresponds to the sample's position in the sample holder, as indicated in Fig. 2.

As the color dots are always above the black ones, the aging kinetics are faster for samples aged in the wind tunnel. Each sample exhibits distinct kinetics: sample no. 2 (brown) shows the fastest kinetics, followed by samples no. 4 and 6. Table 1 shows a wide range of oxidation conditions in terms of temperature and pressure. These different aging conditions could explain the different oxidation levels observed with the color difference. The effects of temperature and static pressure require further investigation. Since both the polymer and composite samples exhibit the same trend of color variation, both types of samples will be analyzed without distinction. Indeed, for both kinds of samples, the color change increases until reaches an asymptotic value. This value is different between the composite samples (40) and the polymer samples (55) because of the fibers. The color measured on the virgin composite sample is darker because the polymer between the fibers is not fully opaque. One consequence of this is that the dispersion is higher than that of the polymer alone, as the average color difference is calculated between the fibers, which can depend on the threshold used to detect the fiber and the polymer matrix.

To determine the faster oxidation, an acceleration factor a is estimated by scaling the aging duration (x-axis) to make the color difference of wind tunnel samples match that of the sample aged in an oven. This scaling time is called equivalent time $t^* = at$. The Figs. 11 and 12 show the variation of the color difference against this equivalent time to illustrate this scaling.

Thus, the equivalent time is the time that the sample should be exposed in the oven condition to obtain the same color difference. If the acceleration factor is greater than 1, the wind tunnel environment accelerates the aging.

4.3. Discussion

Therefore, this part aims to link the accelerating factor, the temperature and the static pressure of the airflow. The Fig. 13 shows the evolution of the acceleration factor for composite (square) and polymer (circle) samples along the position in the sample holder. Each sample undergoes different temperature and pressure conditions.

Then, the effect of the temperature and the pressure is analyzed by establishing a correlation of the acceleration factor a as a function of the temperature of the sample and the static pressure at the interface between the sample and the airflow. If two parameters explain entirely the faster degradation, it means that the airflow affects the oxidation by only changing the temperature and the pressure fields around the sample.

The acceleration factor is estimated for each sample. Fig. 13 shows the acceleration factor a as a function of the position in the sample holder for each sample. On the same plot, the static pressure profile is plotted. A relative good agreement with the pressure seems to be emerging.

The acceleration factor a observed experimentally for aging in the wind tunnel can be decomposed into the product of two contributions:

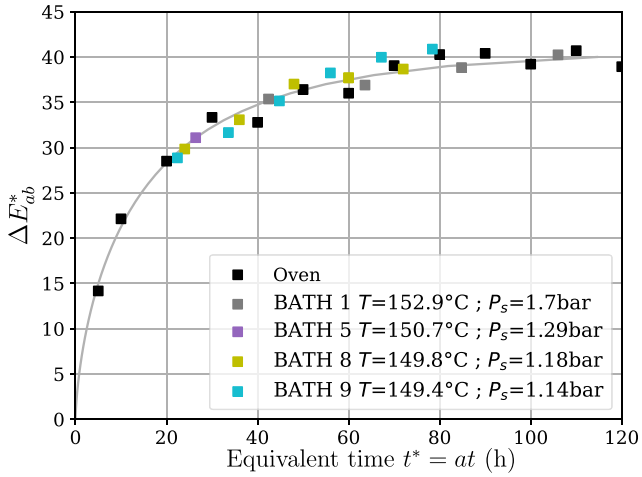

Fig. 11. ΔE^*_{ab} variation against the equivalent time $t^* = at$ on the composite samples. The acceleration factor is chosen to minimize the difference between the oven and the wind tunnel samples.

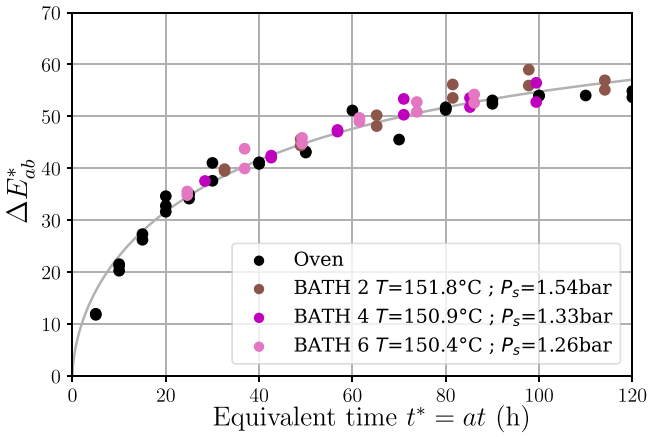

Fig. 12. ΔE^*_{ab} variation against the equivalent time $t^* = at$ on the polymer samples. The acceleration factor is chosen to minimize the difference between the oven and the wind tunnel samples.

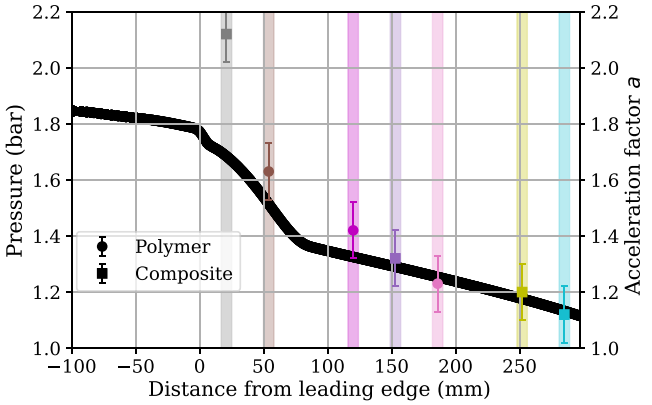

Fig. 13. Comparison between acceleration factor a (colored dot and right y-axis) and the static pressure at the sample surface (black line and left y-axis). Polymer samples are the circle dots and the composite samples are the squared dots.

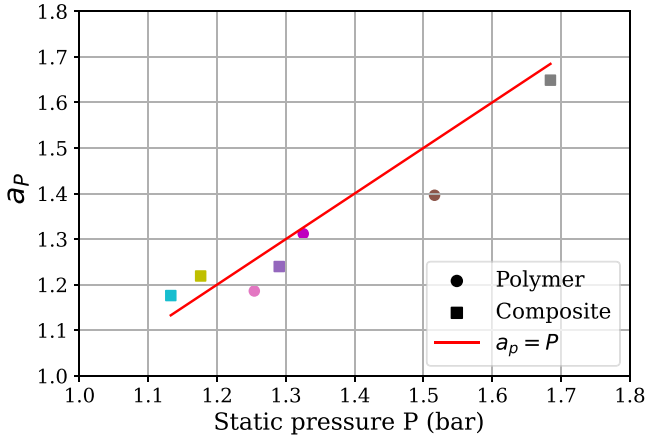

Fig. 14. Variation of the acceleration factor a_P as a function of the static pressure P. The color of the dot is based on their position in the sample older. The circles are for polymer samples and the square for the composite.

temperature (a_T) and pressure (a_P), as described by Eq. (12). This decomposition allows for the differentiation of the effects of temperature and pressure on the acceleration of aging for samples exposed to airflow. While it is possible that additional factors may exist, a factor a_i is introduced. Initially, we assume that only the temperature and the static pressure are significant.

$$a = a_T a_P a_i \tag{12}$$

The influence of temperature is modeled using a time–temperature equivalence correlation [2] (Eq. (13)), with $E_A = 16.290\,\mathrm{kJ\,mol^{-1}}$ and $T_{ref} = 126.5\,°\mathrm{C}$. R is the gaz constant. The parameters E_A and T_{ref} are estimated based on a batch of experimental aging made at various temperature and duration in oven. The activation energy found is the same order of magnitude as values that can be found in the literature [16,40,41].

$$a_T = e^{-\frac{E_A}{R}\left(\frac{1}{T}-\frac{1}{T_{ref}}\right)} \tag{13}$$

Once the contribution of the temperature is known, the contribution of the pressure can be computed. The pressure contribution a_P is defined Eq. (14) as the ratio between the acceleration ratio a estimated experimentally and the contribution of the temperature a_T estimated with Eq. (13).

$$a_P = \frac{a}{a_T} \tag{14}$$

Fig. 14 shows the pressure acceleration factor a_P for each sample depending on the position in the sample holder as a function of the static pressure at the air-sample interface. A linear relationship between the two parameters may be hypothesized. To validate these findings, it is essential to conduct additional experiments that encompass a wider range of airflow conditions and a more diverse selection of polymer types.

The static pressure and the temperature are enough to explain the acceleration of the oxidation inside this aging condition and no other parameters may affect the oxydation in a first order.

With the linear dependency between the static pressure and the accelerating factor a_p and by combining Eqs. (12) and (13), the acceleration factor a for wind tunnel experiments can be expressed as a function of the static pressure of the fluid P, the atmospheric pressure P_0 and the sample temperature T (Eq. (15)), valid for a pressure range between 0 bar and 2 bar.

$$a(T,P) = a_P a_T = \frac{P}{P_0} e^{-\frac{E_A}{R}\left(\frac{1}{T}-\frac{1}{T_{ref}}\right)} \tag{15}$$

The linear dependency of the static pressure means that the oxidation rate is proportional to the oxygen quantity at the interface.

This linear dependency could remain valid only until the saturation of the polymer with oxygen. This linear dependency is fairly valid up to a certain pressure whose value depends on the nature of the polymer [16]. Commonly, the pressure dependence of the oxidation rate is described by a factor β following Eq. (16) where ϕ is the oxidation rate and the subscript 0 denotes the reference conditions.

$$\frac{\phi}{\phi_0} = \frac{1+\beta_0}{\frac{P_0}{P}+\beta_0} \tag{16}$$

For epoxy-based thermosets, β is close to 0.1 but can vary between 0 and 0.5 [16]. The linear dependancy used to describe the variation of a_P in Eq. (14) is Eq. (16) with $\beta = 0$. If we consider $\beta = 0.1$, at $P/P_0 = 1.7$, the oxidation rate increase is estimated at 1.6, which is within our data variability. Our current data are insufficient to determine this parameter β precisely. A study of oxidation in an oven under O_2 partial pressure up to 2 bar or until saturation would be valuable to complete the study and would allow a more relevant discrimination of the influence of the pressure in the wind tunnel.

Therefore, the oxygen boundary condition can be expressed using Henry's law type sorption law, assuming linearity with respect to pressure. Considering the static pressure of the flow P, the boundary condition is given in Eq. (17), where S is the solubility and x_{O_2} is the mole fraction of oxygen in the fluid.

$$[O_2]_0 = S \cdot P \cdot x_{O_2} \tag{17}$$

This boundary condition can be used to estimate the degradation of a composite part over the time under airflow condition and establishes the coupling between the flow via static pressure and the oxygen condition at the interface, essential for describing the oxidation process within the material in the range of pressure tested in this paper.

5. Conclusion

The purpose of this work is to understand the effect of an airflow on the thermo-oxidative aging of the polymer matrix of a composite. To conduct this experimental study, samples were aged in an oven, static air, and in a wind tunnel, dynamic condition. The wind tunnel has been adapted to perform aging at different temperatures and pressures over the different samples tested. First, the roughness measurements showed no erosion on the samples, which means the friction is negligible in this case. Then, the color difference measurements highlighted the faster oxidation kinetics on the samples aged in the wind tunnel. This acceleration is due to the modification of the sample temperature and the static pressure of the airflow. The sample temperature is affected by the airflow because a thermal boundary layer is created that affects convective heat transfer and thus the temperature inside each sample. The static pressure is modified due to the compressible effect.

This work shows that the faster aging can be summarized in an acceleration factor correlation, which is the product of an Arrhenius law on the temperature and a linear law on the static pressure. This linear dependence on static pressure leads to the use of a Henry's law as the oxygen boundary condition. This boundary condition could be used, for example, for modeling purposes.

To design a composite part under airflow, the temperature and pressure fields inside the fluid should be evaluated to accurately know the aging conditions.

These preliminary results could be confirmed by extending these results to a larger pressure range. Other materials could also be investigated to ensure that the behavior of polymers is common for all polymers or if some polymer families have their own behavior.

CRediT authorship contribution statement

Aurélien Doriat: Writing – original draft, Methodology, Investigation, Formal analysis, Conceptualization. **Marco Gigliotti:** Writing – review & editing, Validation, Supervision, Funding acquisition. **Marianne Beringhier:** Writing – review & editing, Validation, Supervision, Funding acquisition. **Gildas Lalizel:** Writing – review & editing, Validation, Supervision, Funding acquisition. **Eva Dorignac:** Writing – review & editing, Validation, Supervision. **Patrick Berterretche:** Writing – review & editing, Supervision, Funding acquisition. **Matteo Minervino:** Writing – review & editing, Supervision, Funding acquisition.

Declaration of competing interest

The authors declare that they have no known competing financial interests or personal relationships that could have appeared to influence the work reported in this paper.

Acknowledgments

This work was supported by SAFRAN Aircraft Engines (50%) and EUR INTREE (50%). This work was supported by the French government program "Investissements d'Avenir" (EUR INTREE, reference ANR-18-EURE-0010). This work pertains to the French government program "Investissements d'Avenir" (LABEX INTERACTIFS, reference ANR-11-LABX-0017-01). The authors thank SAFRAN Aircraft Engines for providing the polymer material.

Data availability

The authors do not have permission to share data.

References

[1] F.-L. Jin, X. Li, S.-J. Park, Synthesis and application of epoxy resins: A review, J. Ind. Eng. Chem. 29 (2015) 1–11, http://dx.doi.org/10.1016/j.jiec.2015.03.026.
[2] M.C. Celina, Review of polymer oxidation and its relationship with materials performance and lifetime prediction, Polym. Degrad. Stab. 98 (12) (2013) 2419–2429, http://dx.doi.org/10.1016/j.polymdegradstab.2013.06.024.
[3] P.-S. Shin, J.-H. Kim, H.-S. Park, Y.-M. Baek, S.-I. Lee, K.L. DeVries, J.-M. Park, A review: Mechanical and interfacial properties of composites after diverse types of aging using micromechanical evaluation, Fibers Polym. 21 (2) (2020) 225–237, http://dx.doi.org/10.1007/s12221-020-9700-7.
[4] A.E. Krauklis, A.T. Echtermeyer, Mechanism of yellowing: Carbonyl formation during hygrothermal aging in a common amine epoxy, Polymers 10 (9) (2018) http://dx.doi.org/10.3390/polym10091017.
[5] J.L. Down, The yellowing of epoxy resin adhesives: Report on high-intensity light aging, Stud. Conserv. 31 (4) (1986) 159–170, http://dx.doi.org/10.2307/1506247.
[6] N. Rasoldier, X. Colin, J. Verdu, M. Bocquet, L. Olivier, L. Chocinski-Arnault, M.C. Lafarie-Frenot, Model systems for thermo-oxidised epoxy composite matrices, Compos. Part A: Appl. Sci. Manuf. 39 (9) (2008) 1522–1529, http://dx.doi.org/10.1016/j.compositesa.2008.05.016.
[7] S. Terekhina, M. Mille, B. Fayolle, X. Colin, Oxidation induced changes in viscoelastic properties of a thermostable epoxy matrix, Polym. Sci. Ser. A 55 (10) (2013) 614–624, http://dx.doi.org/10.1134/S0965545X13090058.
[8] Y. Kobayashi, S. Kobayashi, Accelerated thermo-oxidative aging for carbon fiber reinforced polycyanate under high pressure atmosphere, Adv. Compos. Mater. 26 (5) (2017) 451–464, http://dx.doi.org/10.1080/09243046.2017.1312050.
[9] M. Chipara, M. Chipara, J.R. Romero, Polymer degradation within the glass transition range, Proc. Conf. Electr. Insul. Dielectr. Phenom. - CEIDP '96 2 (1996) 817–820, vol.2.
[10] T.K. Tsotsis, S. Keller, K. Lee, J. Bardis, J. Bish, Aging of polymeric composite specimens for 5000 h at elevated pressure and temperature, Compos. Sci. Technol. 61 (1) (2001) 75–86, http://dx.doi.org/10.1016/S0266-3538(00)00196-2.
[11] X. Colin, F. Essatbi, J. Delozanne, G. Moreau, Towards a general kinetic model for the thermal oxidation of epoxy-diamine networks. effect of the molecular mobility around the glass transition temperature, Polym. Degrad. Stab. 181 (109314) (2020) http://dx.doi.org/10.1016/j.polymdegradstab.2020.109314.
[12] B. Quélennec, R. Delannoy, N. Delpouve, E. Richaud, L. Delbreilh, Acceleration and amplification of physical aging in thermo-oxidized epoxy networks, Macromol. Chem. Phys. 226 (2025).

[13] G.P. Tandon, K. Pochiraju, P.W.R. Beaumont, C.H. Zweben, Environmental durability of polymer matrix composites, 2018, pp. 131–158, http://dx.doi.org/10.1016/B978-0-12-803581-8.10044-X.
[14] T. Tsotsis, Thermo-oxidative ageing of composite materials, Ageing Compos. (2008) 130–159, http://dx.doi.org/10.1533/9781845694937.1.130.
[15] H. Schröder, M. Munz, M. Böhning, A new method for testing and evaluating the long-time resistance to oxidation of polyolefinic products, Polym. Polym. Compos. 16 (2008) 71–79, URL https://api.semanticscholar.org/CorpusID:3576755.
[16] M.C. Celina, E. Linde, M. Barrett, L. Ko, Accelerated oxidation of epoxy thermosets with increased o2 pressure, Polym. Degrad. Stab. (2024).
[17] G. Schoeppner, G. Tandon, K. Pochiraju, Predicting thermooxidative degradation and performance of high-temperature polymer matrix composites, in: Multiscale Modeling and Simulation of Composite Materials and Structures, Springer, 2008, pp. 359–462, http://dx.doi.org/10.1007/978-0-387-68556-4_9.
[18] D. Kondepudi, I. Prigogine, Modern Thermodynamics: From Heat Engines To Dissipative Structures, John Wiley & Sons, 2014.
[19] L. Audouin, V. Langlois, J. Verdu, J. De Bruijn, Role of oxygen diffusion in polymer ageing: kinetic and mechanical aspects, J. Mater. Sci. 29 (3) (1994) 569–583, http://dx.doi.org/10.1007/BF00445968.
[20] J.C. Grandidier, L. Olivier, M.C. Lafarie-Frenot, M. Gigliotti, Modeling the pressure dependent solubility in a thermoset resin for simulating pressure accelerated thermo-oxidation tests, Mech. Mater. 84 (WOS:000352751400004) (2015) 44–54, http://dx.doi.org/10.1016/j.mechmat.2014.09.008.
[21] M.C. Lafarie-Frenot, J.C. Grandidier, M. Gigliotti, L. Olivier, X. Colin, J. Verdu, J. Cinquin, Thermo-oxidation behaviour of composite materials at high temperatures: A review of research activities carried out within the comedi program, Polym. Degrad. Stab. 95 (WOS:000278750800010) (2010) 965–974, http://dx.doi.org/10.1016/j.polymdegradstab.2010.03.019.
[22] W.M. Kays, M.E. Crawford, B. Weigand, Convective Heat and Mass Transfer, vol. 4, McGraw-Hill New York, 1980.
[23] P. Chassaing, Turbulence En Mécanique Des Fluides, Analyse Du Phénomène Dans Une Perspective De Modélisation À L'usage De L'ingénieur, Cépaduès-Editions, 2000.
[24] Y.A. Cengel, Heat and Mass Transfer: A Practical Approach, McGraw-Hill, 2007.
[25] T.H. Chilton, A.P. Colburn, Mass transfer (absorption) coefficients prediction from data on heat transfer and fluid friction, Ind. Eng. Chem. 26 (11) (1934) 1183–1187, http://dx.doi.org/10.1021/ie50299a012.
[26] A. Vedadi, M.S. Parvej, X. Wang, Y. Wang, Comparison of epoxy coating degradations under impingement flow and stationary immersion, in: ASME International Mechanical Engineering Congress and Exposition, Vol. 84508, American Society of Mechanical Engineers, 2020, V003T03A021, http://dx.doi.org/10.1115/IMECE2020-24274.
[27] Q. Zhou, Y. Wang, G.P. Bierwagen, Flow accelerated degradation of organic clear coat: The effect of fluid shear, Electrochim. Acta 142 (2014) 25–33, http://dx.doi.org/10.1016/j.electacta.2014.07.082.
[28] F. Meng, L. Liu, E. Liu, H. Zheng, R. Liu, Y. Cui, F. Wang, Synergistic effects of fluid flow and hydrostatic pressure on the degradation of epoxy coating in the simulated deep-sea environment, Prog. Org. Coat. 159 (2021) 106449, http://dx.doi.org/10.1016/j.porgcoat.2021.106449.
[29] E. Vand der Stok, K. Jacobson, S. Jansma, D. Lukes, Literature review: Effect of clo2 on ageing of polymer materials and related test methods, 2018, pp. 24–26.
[30] N.B. Samarth, P.A. Mahanwar, Degradation of polymer & elastomer exposed to chlorinated water—a review, Open J. Org. Polym. Mater. 11 (1) (2021) 1–50.
[31] A. Doriat, M. Gigliotti, M. Beringhier, G. Lalizel, E. Dorignac, P. Berterretche, M. Minervino, Assessment of a color measurement-based method for the characterization of polymer thermo-oxidation, Polym. Degrad. Stab. (2024) 110950, http://dx.doi.org/10.1016/j.polymdegradstab.2024.110950.
[32] M. Pecora, O. Smerdova, M. Gigliotti, Gradients of cyclic indentation mechanical properties in pr520 epoxy and its 3d carbon fiber composite induced by aging at 150°c, Polym. Degrad. Stab. 193 (2021) 109720, http://dx.doi.org/10.1016/j.polymdegradstab.2021.109720.
[33] A. Subramanian, Contribution To Aerothermal Study of a Film Cooling Geometric Design using Zno Phosphorescence Thermography and Numerical Simulations (Ph.D. thesis), ISAE-ENSMA Ecole Nationale Supérieure de Mécanique et d'Aérotechique - Poitiers, 2022.
[34] F.R. Menter, Two-equation eddy-viscosity turbulence models for engineering applications, AIAA J. 32 (8) (1994) 1598–1605.
[35] N.S. Tomer, F. Delor-Jestin, L. Frézet, J. Lacoste, Oxidation, chain scission and cross-linking studies of polysiloxanes upon ageings, 2012.
[36] Y.-H. Ting, C.-C. Liu, S. min Park, H. Jiang, P.F. Nealey, A.E. Wendt, Surface roughening of polystyrene and poly(methyl methacrylate) in ar/o2 plasma etching, Polymers 2 (2010) 649–663.
[37] X. Colin, F. Essatbi, J. Delozanne, G. Moreau, A new analytical model for predicting the thermal oxidation kinetics of composite organic m atrices. application to diamine cross-linked epoxy, Polym. Degrad. Stab. 186 (2021) 109513, http://dx.doi.org/10.1016/j.polymdegradstab.2021.109513.
[38] D. Rosu, L. Rosu, C.N. Cascaval, Ir-change and yellowing of polyurethane as a result of uv irradiation, Polym. Degrad. Stab. 94 (4) (2009) 591–596, http://dx.doi.org/10.1016/j.polymdegradstab.2009.01.013.
[39] N.S. Allen, M. Edge, S. Hussain, Perspectives on yellowing in the degradation of polymer materials: inter-relationship of structure, mechanisms and modes of stabilisation, Polym. Degrad. Stab. 201 (2022) 109977, http://dx.doi.org/10.1016/j.polymdegradstab.2022.109977.
[40] M.C. Celina, A.R. Dayile, A. Quintana, A perspective on the inherent oxidation sensitivity of epoxy materials, Polymer 54 (13) (2013) 3290–3296, http://dx.doi.org/10.1016/j.polymer.2013.04.042.
[41] M. Celina, E. Linde, D. Brunson, A. Quintana, N. Giron, Overview of accelerated aging and polymer degradation kinetics for combined radiation-thermal environments, Polym. Degrad. Stab. 166 (2019) 353–378, http://dx.doi.org/10.1016/j.polymdegradstab.2019.06.007.